Few-layer Bi_2O_2Se: a promising candidate for high-performance near-room-temperature thermoelectric applications

Weng Hou Yip, Qundong Fu, Jing Wu, Kedar Hippalgaonkar, Zheng Liu, Xingli Wang, Mohamed Boutchich, Beng Kang Tay

Few-Layer Bi_2O_2Se: A Promising Candidate for High-Performance Near-Room-Temperature Thermoelectric Applications

Weng Hou Yip[1,#], Qundong Fu[2,3,#], Jing Wu[4], Kedar Hippalgaonkar[3], Zheng Liu[3], Xingli Wang[2,*], Mohamed Boutchich[2,4,*] and Beng Kang Tay[1,2,*]

[1]Centre for Micro- and Nano-Electronics (CMNE) School of Electrical and Electronics Engineering, Nanyang Technological University, 639798, Singapore (ebktay@ntu.edu.sg);

[2]IRL 3288 CINTRA (CNRS-International-NTU-THALES), Nanyang Technological University, 637553, Singapore;

[3]School of Material Science and Engineering Nanyang Technological University, 639798, Singapore

[4]Institute of Material Research and Engineering, Agency for Science Technology and Research, 138634, Singapore

[5]Sorbonne Universite´, CNRS, Laboratoire de Génie Electrique et Electronique de Paris, 75252, Paris, France

[#]These authors contributed equally to this work

[*]Correspondence and requests for materials should be addressed to B.K Tay (email: ebktay@ntu.edu.sg), M. Boutchich (mohamed.boutchich@sorbonne-universite.fr) or X. Wang (wangxingli@ntu.edu.sg)

Abstract

Advancements in high-temperature thermoelectric materials have been substantial, yet identifying promising near-room-temperature candidates for efficient power generation from low-grade waste heat or thermoelectric cooling applications has become critical but proven exceedingly challenging. Bismuth oxyselenide (Bi_2O_2Se) emerges as an ideal candidate for near-room-temperature energy harvesting due to its low thermal conductivity, high carrier mobility and remarkable air-stability. In this study, the thermoelectric properties of few-layer Bi_2O_2Se over a wide temperature range (20 – 380 K) are investigated, where a charge transport mechanism transitioning from polar optical phonon (POP) to piezoelectric scattering at 140 K is observed. Moreover, the Seebeck coefficient (*S*) increases with temperature up to 280 K then stabilizes at ~ -200 μV/K through 380 K. Bi_2O_2Se demonstrates high mobility (450 $cm^2V^{-1}s^{-1}$) within the optimum power factor (*PF*) window, despite its $T^{-1.25}$ dependence. The high mobility compensates the minor reduction in carrier density n_{2D} hence contributes to maintain a robust electrical conductivity $\sim 3x10^4$ S/m. This results in a remarkable *PF* of

860 μW $m^{-1}K^{-2}$ at 280 K without the necessity for gating (V_g = 0 V), reflecting the innate performance of the as-grown material. These results underscore the considerable promise of Bi_2O_2Se for room temperature thermoelectric applications.

1. Introduction

Thermoelectric (TE) materials are capable of directly transforming the heat energy absorbed into electrical energy, alleviating the damages on environment due to the rapid consumption of fossil fuels to satisfy the high energy demand. Moreover, TE generators have garnered significant attention due to its unparalleled advantages, including generation of electrical energy in the absence of physical moving parts, eco-friendliness (silent operation) and long service life (low maintenance cost)[1]. Recent advancements in room-temperature thermoelectric materials have showcased their potential for diverse applications including power generation, sensing, and thermal management. Innovations include integrated systems that combine solar absorbers, radiative coolers, and thermoelectric generators to convert thermal energy from various sources into electricity, offering a sustainable alternative to fossil fuels[2]. Additionally, microscale thermoelectric devices (micro-TEDs) have been developed with enhanced microfabrication techniques, improving performance and durability while enabling sensitive environmental monitoring[3]. These developments highlight the versatility of room-temperature thermoelectric materials in seamlessly integrating into everyday devices and industrial systems, significantly enhancing energy efficiency across various applications.

The power generation efficiency can be evaluated through a dimensionless figure of merit *ZT*, defined as $ZT = S^2\sigma T/\kappa$; S is the Seebeck coefficient, defined as $S = -\Delta V/\Delta T$ where ΔV is the thermoelectric voltage generated and ΔT is the temperature difference at the two extremities of the TE material, σ is the electrical conductivity, T is the absolute temperature and κ is the sum of electronic thermal conductivity (κ_e) and lattice thermal conductivity (κ_L)[4-7]. In addition to *ZT*, the power factor ($PF = S^2\sigma$) serves as a crucial metric that underscores a material's potential for efficient energy conversion. The power factor directly impacts the power output of thermoelectric devices, making it an essential consideration in applications where maximizing immediate energy conversion from limited heat sources is a priority. This characteristic is especially critical in designing materials that are not only efficient but also capable of generating substantial power under practical operating conditions. It is obvious that by increasing S and σ while minimizing κ should ideally increase *ZT*, however, these parameters are interdependent which makes it challenging to obtain a high *ZT*[8, 9]. For example, increasing the carrier concentration (*n*) will lead to an increase in σ and κ_e but results in a decrease of S. Low dimensional material have attracted attention and the quantum confinement taking place at such scale can be beneficial to enhance the efficiency of thermoelectric materials[10]. Over the past few decades, numerous strategies have been employed to optimize the *ZT* value by decoupling its numerator and denominator. These approaches encompasses band convergence, anharmonicity, modulation doping[11] to increase the σ as well as the introduction of lattice defects[12-14] to reduce

κ. Moreover, the prevalence of interfaces and disparities in mass among the constituent atoms in certain 2D materials can result in comparatively reduced κ[15, 16]. Lee *et al.*[17] observed a negative correlation between κ and σ in tin disulfide (SnS_2) while scaling the material from bulk to 2D nanosheets substantially increasing the thermoelectric performance. In that regard, two-dimensional (2D) semiconducting materials with distinctive density of states can achieve significant Seebeck coefficients. This characteristic is crucial as it directly amplifies their *PF*, which correlates with the maximum power output a material can achieve. It is important to emphasize that achieving a high *PF* is essential because the ZT value, while indicating overall thermoelectric performance, does not reflect the maximum power output that is achievable[18].

The layered bismuth oxychalcogenides (Bi_2O_2X) materials such as (Bi_2O_2S, Bi_2O_2Se and Bi_2O_2Te) stood out due to its unparalleled properties of remarkable air stability, tunable band structures, high carrier mobilities and low thermal conductivity which are desired for high thermoelectric performance[19]. Among the three Bi_2O_2X, Bi_2O_2Se have been proven to be the easiest to grow due to its stable chemical potential. Particularly, 2D Bi_2O_2Se exhibits high mobility and suitable bandgap of about 0.8 eV[20] which have been predicted to be a promising thermoelectric material[21]. For example, Wu *et al.* noted an ultrahigh Hall mobility exceeding 20,000 $cm^2V^{-1}s^{-1}$ at low temperatures[22], while Guo *et al*. [23] calculated and measured the anisotropy of thermal conductivity between through-plane and in-plane as a function of the thickness owing to the electrostatic interactions between layers in ferroelectric Bi_2O_2Se. Their findings revealed that the κ did not exceed 1.5 W $m^{-1}K^{-1}$ for thickness up to 20 nm, that is as low as silicon oxide (SiO_2). Moreover, Yang et al. reported a high-power factor as high as 400 μW $m^{-1}K^{-2}$ by manipulating the scattering mechanisms over a temperature range of 80-200 K[24], however the performance around room temperature is still lacking. These state-of-the-art references will be our benchmark for this work.

In this study, we characterize the electrical transport and *PF* of Bi_2O_2Se in its 2D form (∼14 nm) over a wide temperature range (20 – 380 K). We measured a large variation of the electric mobility over this temperature range and observe a clear transition from POP to piezoelectric scattering regimes at 140 K. Despite the power dependence $T^{-1.25}$ of the mobility and that the σ (∼10^4 S/m) decreases with temperature from decreasing carrier concentration, the mobility remains substantially high at ∼450 $cm^2V^{-1}s^{-1}$ at 280 K with a Seebeck coefficient that plateaus at approximately –200 μV/K thereafter. As a result, we achieve a peak *PF* of 860 μW $m^{-1}K^{-2}$ near room temperature operation without the necessity of gating (V_g = 0V). These orders of magnitude are several folds larger than recent reports[24]

and highlights the potential of as deposited Bi_2O_2Se as a candidate for a large range of TE application such as remote sensing, imaging or thermoelectric generators, especially at room temperature.

2. Materials and methods

2.1. LPCVD synthesis of Bi_2O_2Se

The setup for the low-pressure chemical vapor deposition (LPCVD) synthesis of Bi_2O_2Se on fluorine mica substrate (f-mica, $KMg_3(AlSi_3O_{10})F_2$) involves a split tube furnace equipped with an interconnected control system (1-Zone, up to 1200 °C). Fused quartz tubes measuring 1200 mm in length and 50 mm in outside diameter (O.D.) were employed. Precursors, namely powders of Bi_2Se_3 and Bi_2O_3, were positioned in separate alumina crucibles. Bi_2O_3 was placed in the central zone, while Bi_2Se_3 was positioned upstream at 8 cm. The f-mica substrate was situated downstream with a separation of 12 cm. Initially, the chamber was evacuated to 6.0×10^{-2} Torr, following which 170 sccm (standard cubic centimeter per minute) of Argon (Ar) gas was introduced to achieve a pressure within the range of 350–400 Torr. The chamber was then gradually heated to 620 °C over a span of 25 minutes and maintained at this temperature for 40 minutes. Subsequently, the furnace was allowed to cool naturally to room temperature, and the chamber was replenished with Ar gas to return to atmospheric pressure.

2.2. Characterization of Bi_2O_2Se

Atomic force microscopy (AFM) was performed using the Asylum Research Cypher Scanning Probe Microscope system in tapping mode. Raman spectra were acquired using the Witec Raman system equipped with a 100x objective lens, a grating of 1200 lines mm^{-1} and a Rayleigh peak filter, employing 532 nm laser excitation. The transmission electron microscopy (TEM) samples were prepared using a polymethyl methacrylate (PMMA)-based transfer method. Initially, the f-mica substrates with the as-grown CVD samples were spin-coated with PMMA at 3000 r.p.m. for 60 seconds, followed by baking at 150 °C for 5 minutes. Subsequently, the PMMA-coated sample was carefully peeled off by etching away the underlying f-mica using a 2% hydrofluoric (HF) solution. Next, the floating PMMA film was delicately transferred to DI water and lifted onto a TEM grid. The TEM grid was then dried at 50 °C for 30 minutes and immersed in acetone for approximately 24 hours to remove the PMMA. Finally, the TEM grid was rinsed with isopropyl alcohol (IPA) and air-dried for further analysis.

2.3. Transfer method

The transfer of as-grown Bi_2O_2Se onto a Si substrate utilized a polystyrene (PS)-assisted approach. Initially, PS was spin-coated onto the f-mica substrate containing the Bi_2O_2Se at 3500 r.p.m. for 60 seconds and then baked at 85 °C for 15 minutes. Following this, the edge of the f-mica was trimmed, and the PS-coated sample was gently separated using a drop of DI water. Subsequently, the detached PS film was meticulously placed onto the Si substrate. The Si substrate was dried at 80 °C for 1 hour and then subjected to a 150 °C heating for 30 minutes to enhance the contact between the sample and the Si substrate. Next, the Si substrate was immersed in dimethylformamide (DMF) solution for 24 hours to remove the PS, followed by a 5-hour immersion in acetone to eliminate any remaining organic residues. Finally, the Si substrate was dried using a stream of floating nitrogen.

2.3. Device fabrication and measurement method

Upon transferring Bi_2O_2Se onto the Si substrate, a layer of PMMA was spin-coated onto the sample. Following this, electrode patterns were defined using electron-beam lithography (EBL) carried out on the ZEISS EVO 10. After the pattern development in methyl isobutyl ketone (MIBK)/IPA, metal contacts (10 nm Ti/80 nm Au) were deposited using the AJA electron beam evaporator. To characterize the electrical properties of the FETs, the Agilent B1500A Semiconductor Device Parameter Analyzer within the MicroXact Probe Station.

To measure the Seebeck coefficient, we established a temperature gradient by passing a DC current bias through the micro-heater using a source-meter (Keithley 6221). This setup induced Joule heating, creating a temperature gradient along the sample. The temperature gradient, in turn, generated a thermoelectric voltage, which we measured using a voltmeter (Keithley 6430). As we applied a series of DC current biases with increasing values to the heater, we recorded the corresponding voltages. The temperature gradient was determined by measuring the 4-probe resistance of the thermometers.

3. Results and discussions

3.1. Structural analysis

Bi_2O_2Se crystallizes with a tetragonal phase(I4/mmm, $a = 3.891$ Å, $c = 12.21$ Å and $Z = 2$)[25]. In the crystal cell as shown in Figure 1a, each oxygen atom is covalently bonded with four bismuth atoms, forming a Bi_4O tetrahedron. The tetrahedrons that share edges are arranged together which configures a positively charged $[Bi_2O_2]_n^{2n+}$ layer. Meanwhile, the negatively charged $[Se]_n^{2n-}$ layer along with the upper and lower $[Bi_2O_2]_n^{2n+}$ layer are held together by weak electrostatic force, forming an

interlayer spacing of roughly 0.61 nm. High-quality Bi_2O_2Se on 300 nm SiO_2/Si substrate are prepared with LPCVD method (Figure 1b) followed by a non-corrosive transfer method[25]. Generally, Bi_2O_3 and Bi_2Se_3 powders used as precursors are placed apart in different crucibles upstream of the quartz tube and positioned in the high-temperature zone. Argon gas is used to aid vapor transport to the growth substrate (f-mica) which is positioned downstream of the quartz tube. The quartz tube is held at low-pressure throughout the growth of Bi_2O_2Se. The synthesized samples are usually squares in shape with lateral size over 50 μm (Figure 1c). Such morphology indicates the tetragonal crystal group of Bi_2O_2Se. Raman spectroscopy is an effective method to confirm the phase of the Bi_2O_2Se flakes. In Figure 1d, an obvious peak observed at 159.1cm^{-1} in the Raman spectrum matches well with the A_{1g} peak of Bi_2O_2Se in past reports[26, 27]. The topography and the thickness of the as-grown sample were determined through atomic force microscopy (AFM, Figure 1e) where the surface is clean and flat with a thickness of 14.9 nm. The crystal structure of the as-grown Bi_2O_2Se samples was further confirmed using scanning transmission electron microscopy (STEM). The annular dark-field (ADF) imaging conducted on an aberration-corrected STEM image (Figure 1f) reveals a *d*-spacing of 0.28 nm for the (110) plane of few-layer Bi_2O_2Se, signifying the pristine quality of the samples. Furthermore, Figure 1g shows the fast Fourier transform (FFT) of Figure 1f which showcases $(1\bar{1}0)$, (110), and (200) spots arranged in a square pattern, confirming the single-crystalline nature of the Bi_2O_2Se flakes.

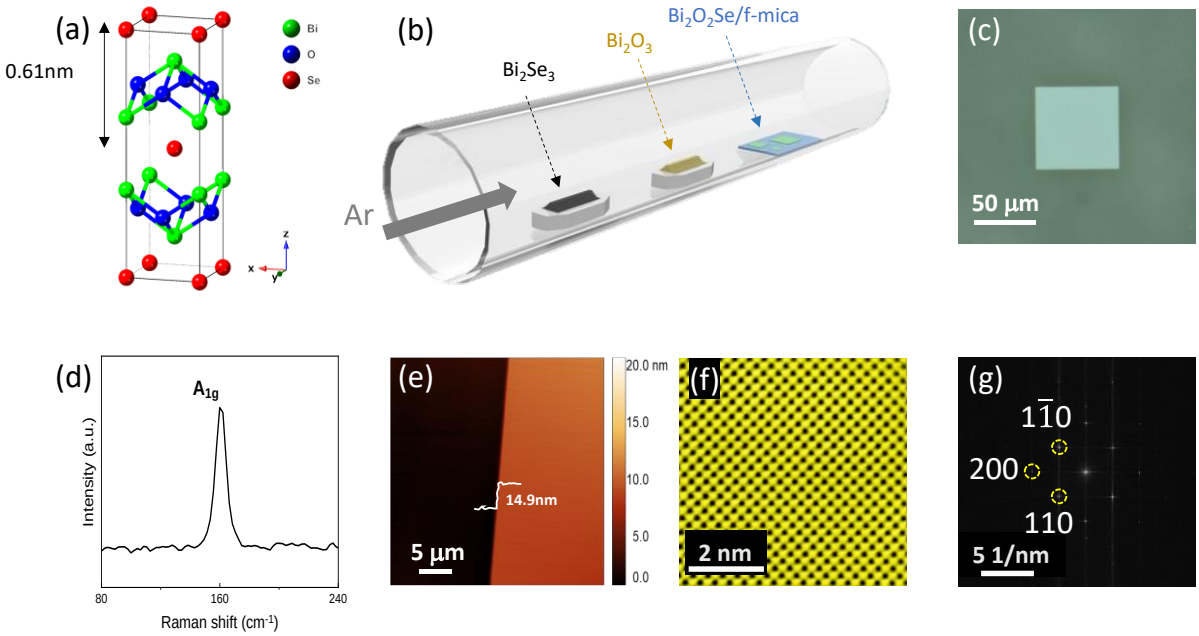

Figure 1. LPCVD synthesis and characterization of Bi_2O_2Se. a) Layered crystal structure of Bi_2O_2Se. b) Schematic of the LPCVD setup for the synthesis of Bi_2O_2Se. c) Optical image of square Bi_2O_2Se on f-mica with domain size larger than 50 μm. d) Raman spectra of Bi_2O_2Se with the characteristic A_{1g} peak at 159.1 cm^{-1}. e) AFM image of as-grown Bi_2O_2Se on f-mica with a thickness of 14.9 nm. f) ADF-STEM image of Bi_2O_2Se. g) FFT of Figure 1f, indicating the crystal group of *I4/mmm*.

In this work, PS-assisted transfer method (Supplementary Figure 1) is adopted to transfer Bi_2O_2Se flakes onto a desired working substrate; here a SiO_2/Si substrate is used where the thickness of SiO_2 is 300nm. This method is preferred over the PMMA-assisted transfer method due to an absence of an etching step. In PMMA-assisted transfer method, HF acid is required to etch away the underlying growth substrate (f-mica) which can be detrimental to the Bi_2O_2Se flakes[25] and its electronic properties. Hence, a non-corrosive transfer method such as PS-assisted transfer method is highly desired as demonstrated by the transport properties exhibited in the following sections.

3.2. Electrical properties

To study the electrical and the thermoelectric performances of the samples, a fanout micro-test structure was fabricated on the Bi_2O_2Se flake (Figure 2a), which is commonly used for thermoelectric measurements on 2D and 1D materials[28-30]. The test structure includes a micro-heater that is not in direct contact with the sample which purpose is to create a lateral temperature gradient through Joule heating. The Ti/Au lines connected to the sample function as the source or drain electrodes for electrical transport measurements and as local resistive thermometers. The performance of the device hinges significantly on post-fabrication treatments, and annealing is well-known to reduce contact resistance between 2D materials and metal electrodes, which is pivotal for ensuring efficient electron flow between the electrodes and the 2D flakes. In this case, we performed an annealing step – subjecting the device to a temperature of 380 K for 4 hours within an ultrahigh vacuum environment ($p \approx 1 \times 10^{-7}$ mbar). Validating our approach, post-annealing results were quite telling: the two-probe resistance experiences a reduction from a rather high resistance of 3.49 MΩ to a much lower resistance of 1.95 kΩ (Supplementary Figure 2) when a back gate voltage of 60 V was applied. This drastic change is also attributed to the result of electrostatic doping moving the fermi-level (E_F) closer to conduction band minima (CBM) which increases the carrier concentration and consequently reducing resistance.

Next, we characterize the electrical properties of Bi_2O_2Se device through two-probe measurement to obtain the transfer characteristics (I_d - V_g) as shown in Figure 2b. An essential observation was the manifestation of n-type transport, a characteristic often seen in semiconductors where the primary charge carrier is an electron. Notably, the maximum-to-minimum current ratio is $I_{max}/I_{min} \approx 10^5$ at room temperature (300 K). Shedding light on the finer details, Figure 2c and 2d highlight the conductivity's variation concerning both back gate voltage and temperature which are crucial in understanding the inherent properties of semiconductors. For high-precision measurements, a four-probe configuration (Supplementary Figure 3) was employed. This approach effectively bypasses the

issues of contact resistances that can introduce errors in readings. The measurements revealed a notable trend where the conductivity decreased as the temperature increased, suggesting the sample's metallic properties or its behavior as a degenerate semiconductor. From the conductance versus temperature measurement, the carrier density n_{2D} is extracted (Supplementary Figure 4) and we note that the carrier density is higher at low temperature. Furthermore, the field-effect mobility was obtained by fitting the linear region of the four-probe transfer curve through the equation $\mu = \frac{1}{C_{ox}} \times \frac{L}{W} \times \frac{dG}{dV_g}$ where C_{ox} is the capacitance of the dielectric layer (300 nm thick SiO_2), *G* is the channel conductance, *L* and *W* is the length and width of the channel respectively. To understand the scattering mechanism, μ is plotted as a function of temperature and fitted with a power-law relationship of $\mu \sim T^{-\gamma}$ as shown in Figure 2e. Typically, at elevated temperature (exceeding 100 K), μ is primarily constrained by either acoustic phonon (AP) or optical phonon (OP) scattering[31-34]. AP scattering occurs when charge carriers are disrupted by low-energy lattice vibrations, like sound waves. Conversely, OP scattering is caused by high-energy, short-lived lattice vibrations akin to optical light frequencies. With decreasing temperature, the vibrational motion of phonons diminishes, making room for ionized impurity scattering to become predominant factor in the charge transport. This shift results in a reduction or plateauing of μ as the temperature continues to decrease. However, instead of transitioning into the ionized impurity scattering regime, the μ of our Bi_2O_2Se sample continues to increase with a milder slope ($\gamma = -0.19$) as the temperature decreases below 140 K[24]. This is owing to the polar nature of ferroelectric properties of Bi_2O_2Se where piezoelectric scattering becomes dominant below 140 K, following a temperature dependence of $T^{-0.19}$. In a piezoelectric material below a certain temperature threshold (such as Bi_2O_2Se below 140 K), the piezoelectric effect can counteract the negative impact of ionized impurity scattering. The piezoelectrically-induced electric field counterbalance with the fields from the ionized impurities in such a way that it reduces their effectiveness in scattering charge carriers. Essentially, the piezoelectric field can "screen" or reduce the impact of the Coulombic fields caused by ionized impurities, resulting in maintenance or enhancement in μ[35].

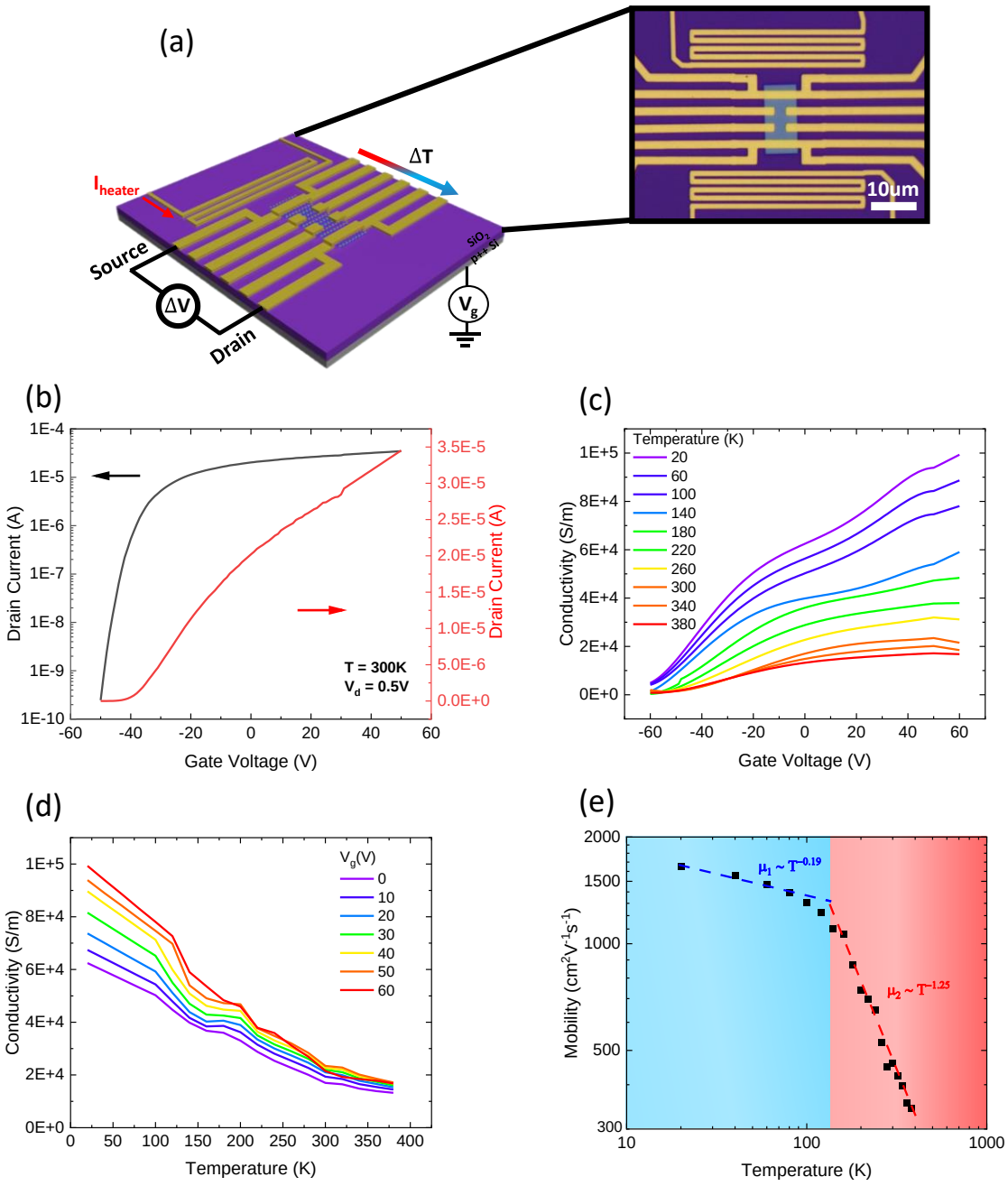

Figure 2. Electrical transport measurements of Bi_2O_2Se. a) Schematic illustration of fan-out micro-test structure on Bi_2O_2Se for thermoelectric measurements. b) Two-probe transfer characteristic (I_d vs V_g) of Bi_2O_2Se. c) Four-probe electrical conductivity plotted against V_g for various temperature. d) Four-probe electrical conductivity plotted against temperature for various V_g. e) FET mobility plotted against temperature, blue region indicates piezoelectric-dominant scattering regime below 140 K and red region indicates POP-dominant scattering regime above 140 K.

3.3. Thermoelectric properties

To capture the thermoelectric transport of Bi_2O_2Se, its electrical conductivity (σ) and Seebeck coefficient (S) were measured across a wide temperature range from 20 K to 380 K while applying different gate voltages. The Seebeck coefficient, defined as $S = -\Delta V/\Delta T$, essentially measures how much voltage is produced for a given temperature difference. This metric provides a crucial window

into the intrinsic thermoelectric behavior of a material. The process of measurement is methodical and split into two main parts: measurement for ΔV and ΔT, respectively. Before the measurement of ΔT (Supplementary Figure 5), the Ti/Au resistive thermometers at the two extremities of the sample must be calibrated by measuring their temperature coefficient of resistance (TCR). Next, the sample is subjected to a lateral temperature difference through Joule heating of the micro-heater. This temperature difference is then quantified with the help of the calibrated TCR values of the two resistive thermometers. We then proceed to measure the induced ΔV (Supplementary Figure 6) across the Bi_2O_2Se to calculate S and plotted it as a function of temperature as shown in Figure 3a. Evidently, the negative polarity of S indicates carrier transport of electrons which aligns with the n-type transport observed from the transfer characteristics in Figure 2b. Moreover, the increase in S with decreasing carrier density and temperature resonates with the characteristics of a semiconducting material[36]. The rise in S continues until it plateaus at a maximum ~ -200 µV/K from 280 K onwards which is attributed to the balance reached between carrier energy and scattering mechanisms. At lower temperatures, an increase in thermal energy leads to more active carriers, enhancing *S*. As the temperature continues to rise beyond 280 K, additional thermal excitations result in increased carrier scattering, such as phonon scattering, which tends to decrease mobility and can offset gains in *S* from increased carrier energy, leading to a saturation point. Moreover, by leveraging Nano Angle-Resolved Photoemission Spectroscopy (nano-ARPES), an advanced tool allowing us to examine electronic structures, we discern the Fermi level (E_F) nestling within an electron pocket at the Γ point, as illustrated in Supplementary Figure 7. In the case of Bi_2O_2Se, as indicated by the nano-ARPES findings, the Fermi level positioning within an electron pocket can lead to a high density of states at the Fermi level. A sharp peak in the density of states around the Fermi level can enhance the *S*[10]. This observation not only aligns with the general principles of condensed matter physics but further cements Bi_2O_2Se's status as a degenerated semiconductor with an impressively elevated *S*.

The Seebeck coefficient, which illuminates the thermoelectric behavior of materials, can be mathematically framed using a well-accepted model based on Boltzmann statistics. In this context, the expression for Seebeck is represented as $S = \pm\frac{k_B}{q}(ln\sigma - ln\sigma_0)$. This equation is rooted in the statistical mechanics of thermoelectric behavior and speaks to how electron or hole concentrations shift with temperature, affecting the voltage change for a given temperature gradient. Here, the symbols "+" and "–" respectively denote n-type and p-type semiconductors, denoting whether the primary charge carriers are electrons or holes[37]. The parameters k_B and q represent Boltzmann's constant and the elementary charge of an electron, respectively. The ratio $\frac{k_B}{q}$ translates to 86.15 µV/K

for phonon-dominated scattering which is also typically used as a guide for the eye as shown in the Jonker plot (S vs $ln\sigma$) in Figure 3b. We observed that the slope of the line in the Jonker plot closely aligns with the expected slope of 86.15 µV/K for temperatures exceeding 140 K (red region), indicating a phonon-dominated scattering regime. However, for temperatures below 140 K (blue region), an anomalous trend emerges as the slope of the line starts to deviate. This is likely due to a decoupling between S and σ, where there is no substantial decrease in S despite a sharp increase in σ. Such an observation suggests that the enhanced conductivity is not primarily driven by changes in carrier concentration. Instead, it arises from a notable boost in carrier mobility owing to the piezoelectric scattering regime, which does not influence the Seebeck coefficient. Supporting this, our conductance versus temperature measurement (refer to Supplementary Figure 4) reveals a higher carrier density n_{2D} at lower temperatures. Yet, the mobility continues to rise, explaining the amplified conductivity in this temperature bracket.

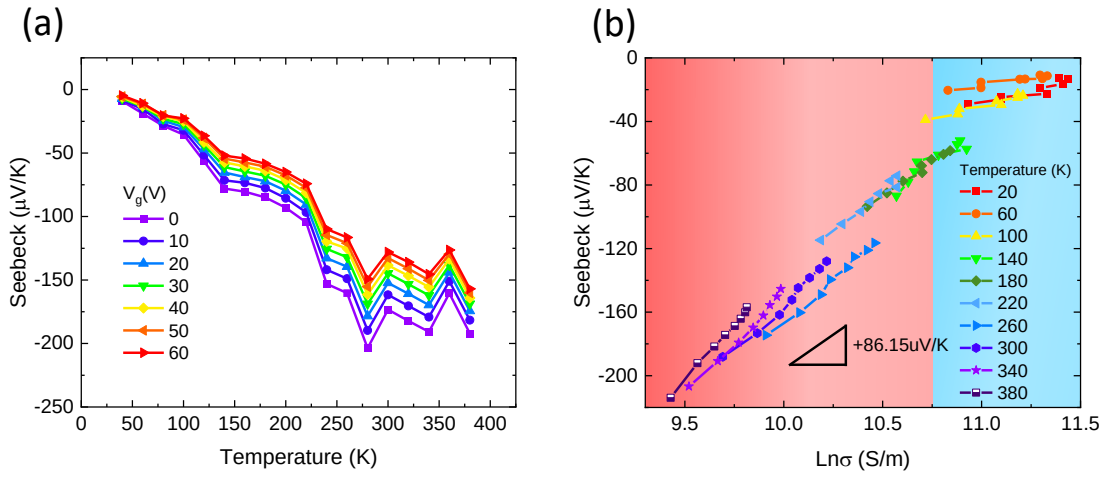

Figure 3. Thermoelectric transport measurement of Bi_2O_2Se. a) Seebeck coefficient plotted against temperature for various V_g. b) Typical Jonker plot where Seebeck coefficient is plotted against Lnσ. $\frac{k_B}{q} = 86.15\ \mu V/K$ is shown as guide for the eye. Red region indicates the slope of the line aligning to the standard slope $86.15\ \mu V/K$ above 140 K while blue region indicates the slope of the line deviating from it below 140 K.

In the realm of thermoelectric materials, the interplay between and σ and *S* is crucial, especially when analyzing the power factor *PF* = $S^2\sigma$, which fundamentally drives the efficiency of a material's ability to convert thermal energy into electrical energy. As shown in Figure 4a, while the σ rises with an increase in carrier density, the magnitude of S follows the opposite trend. This is a typical behavior since having more charge carriers available in a material aid in the conduction of electrical currents. On the other hand, the *S* decreases when the carrier density is high as individual carriers have a reduced average energy difference between the hot and cold ends[38]. In other words, with more carriers sharing the thermal energy, each carrier contributes less to the total voltage difference,

causing a decrease in *S*. This effect is accentuated as the gate voltage increases; as E_F shifts closer to CBM and the net contribution from carriers with energy beyond and below the vicinity of E_F diminishes, leading to a lower S[39]. To obtain a more comprehensive understanding of the material's overall thermoelectric performance, we consider the dependence of *PF* on temperature. As σ increases with temperature, the influx of additional charge carriers into the channel initially boosts the *PF*, reaching a peak at 280 K, corresponding to a carrier mobility of ~450 $cm^2V^{-1}s^{-1}$. This point aligns with where *S* begins to plateau (Supplementary Figure 8) even as conductivity declines due to reduced carrier density. Beyond 280 K, *PF* starts to decrease as the μ enters the POP regime leading to reduced μ. Given that the power factor (*PF*) is defined as ($PF = S^2\sigma$), even if the *S* remains constant or changes insignificantly, the overall power factor will decrease due to the diminished conductivity resulting from reduced μ in the POP regime. The *PF* is plotted against the temperature in Figure 4b for each gate voltage. A peak *PF* value of 860 $\mu W\ m^{-1}K^{-2}$ is achieved at 280 K when no gate voltage is applied. Figure 4c was plotted to explicitly display the effectively conditions where high *PF* can be obtained. Remarkably, the *PF* above 500 $\mu W\ m^{-1}K^{-2}$ can be maintained from 230 K to 330 K without a need to apply gate voltage. It implies that the material inherently possesses optimal thermoelectric properties, reducing the need for external control or adjustments, which can complicate device design and implementation. At room temperature (300 K), our Bi_2O_2Se sample displays a record high *PF* of 578 $\mu W\ m^{-1}K^{-2}$ as compared to other reports on few-layer[24], bulk[40-44], nanostructured and doped Bi_2O_2Se[45] (Figure 4d).

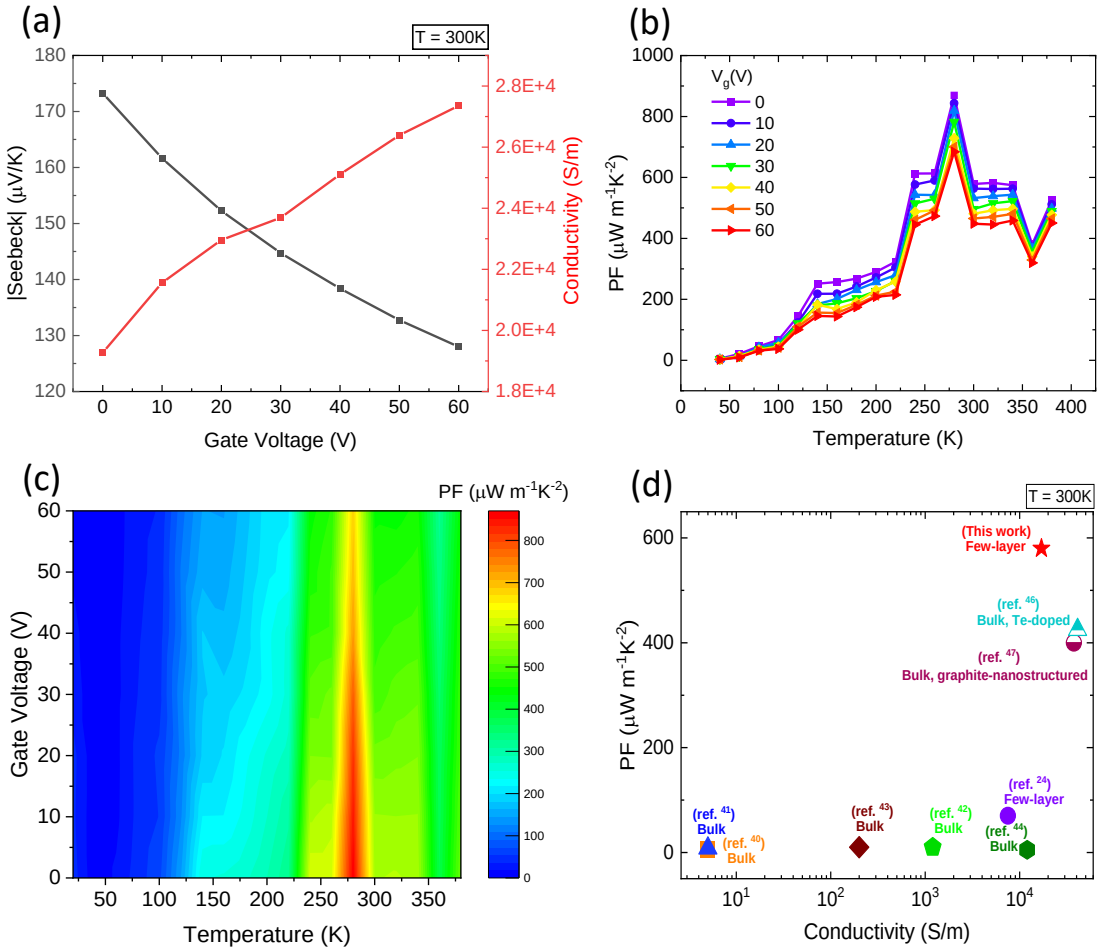

Figure 4. Thermoelectric performance of Bi_2O_2Se. a) Power factor plotted against temperature for various V_g. b) Seebeck coefficient and electrical conductivity plotted against V_g at 300K. c) Colour contour plot of power factor versus V_g and temperature. d) Comparison of power factor with other works on few-layer[24], bulk[40-44], $Bi_2O_{1.96}Te_{0.04}Se$[46] and Bi_2O_2Se-0.5% mol graphite[47] at 300K.

4. Summary

In summary, our extensive investigation into the thermoelectric properties of few-layer Bi_2O_2Se, facilitated by modulating charge densities via back gate voltage across a wide temperature range (20 – 380 K), has been greatly enhanced using the PS-assisted transfer method. This method has ensured the high quality of our Bi_2O_2Se samples, which is a critical factor contributing to their impressive thermoelectric performance.

Our study identified two distinct scattering regimes: piezoelectric scattering, which is predominant below 140 K, and POP scattering above this temperature. Despite a $T^{-1.25}$ temperature dependence observed above 140 K, we recorded a high mobility of 450 $cm^2V^{-1}s^{-1}$ at 280 K, and the Seebeck coefficient plateauing at a high value of approximately -200 μV/K. This culminated in achieving the

highest reported *PF* of 860 μW $m^{-1}K^{-2}$ for Bi_2O_2Se at temperatures near room level, notably achieved without the need for electrostatic gating.

The significance of this high *PF*, particularly at near-room temperatures, positions Bi_2O_2Se as an exceptionally promising candidate for practical applications in room-temperature waste heat harvesting. This high *PF* near ambient temperatures opens new possibilities to efficiently convert waste heat into electrical energy, which is highly desirable, particularly in areas such as temperature sensing and thermoelectric generators.

Acknowledgements

Funding: This research was supported by the Ministry of Education (MOE), Singapore under Grant MOE-T2EP50221-0003.

Data availability statement

All data needed to evaluate the conclusions in the paper are present in the paper and/or the Supplementary Materials. Additional data related to this paper may be requested from the authors.

Credit authorship contribution statement

W.Y., Q.F., X.W, M.B. and B.T. conceived and designed the project. W.Y. and Q.F. performed material synthesis, device fabrication, electrical and thermoelectric measurements. Q.F. contributed to material characterization. W.Y., Q.F., X.W., M.B., G.Z. and J.W. analyzed the data. W.Y., Q.F., M.B. and X.W. drafted the manuscript. All authors discussed and commented on the manuscript.

Declaration of competing interest

The authors declare no competing interests.

References

[1] N. Sugiartha and P. Sastra Negara, "Technical Feasibility Evaluation on The Use of A Peltier Thermoelectric Module to Recover Automobile Exhaust Heat," *Journal of Physics: Conference Series,* vol. 953, p. 012090, 2018/01 2018, doi: 10.1088/1742-6596/953/1/012090.

[2] S. Zhang, Z. Liu, X. Zhang, Z. Wu, and Z. Hu, "Sustainable thermal energy harvest for generating electricity," *The Innovation,* vol. 5, no. 2, p. 100591, 2024/03/04/ 2024, doi: https://doi.org/10.1016/j.xinn.2024.100591.

[3] Z. Liu *et al.*, "High-performance integrated chip-level thermoelectric device for power generation and microflow detection," *Nano Energy,* vol. 114, p. 108611, 2023/09/01/ 2023, doi: https://doi.org/10.1016/j.nanoen.2023.108611.

[4] Y. Xiao and L.-D. Zhao, "Seeking new, highly effective thermoelectrics," *Science,* vol. 367, no. 6483, pp. 1196-1197, 2020, doi: doi:10.1126/science.aaz9426.

[5] J. P. Heremans *et al.*, "Enhancement of Thermoelectric Efficiency in PbTe by Distortion of the Electronic Density of States," *Science,* vol. 321, no. 5888, pp. 554-557, 2008, doi: doi:10.1126/science.1159725.

[6] Y. Pei, X. Shi, A. LaLonde, H. Wang, L. Chen, and G. J. Snyder, "Convergence of electronic bands for high performance bulk thermoelectrics," *Nature,* vol. 473, no. 7345, pp. 66-69, 2011/05/01 2011, doi: 10.1038/nature09996.

[7] A. I. Hochbaum *et al.*, "Enhanced thermoelectric performance of rough silicon nanowires," *Nature,* vol. 451, no. 7175, pp. 163-167, 2008/01/01 2008, doi: 10.1038/nature06381.

[8] G. J. Snyder and E. S. Toberer, "Complex thermoelectric materials," (in eng), *Nat Mater,* vol. 7, no. 2, pp. 105-14, Feb 2008, doi: 10.1038/nmat2090.

[9] T. Zhu, Y. Liu, C. Fu, J. P. Heremans, J. G. Snyder, and X. Zhao, "Compromise and Synergy in High-Efficiency Thermoelectric Materials," *Advanced Materials,* vol. 29, no. 14, p. 1605884, 2017, doi: https://doi.org/10.1002/adma.201605884.

[10] L. D. Hicks and M. S. Dresselhaus, "Effect of quantum-well structures on the thermoelectric figure of merit," *Physical Review B,* vol. 47, no. 19, pp. 12727-12731, 05/15/ 1993, doi: 10.1103/PhysRevB.47.12727.

[11] J. He and T. M. Tritt, "Advances in thermoelectric materials research: Looking back and moving forward," *Science,* vol. 357, no. 6358, p. eaak9997, 2017, doi: doi:10.1126/science.aak9997.

[12] Y. Zhao *et al.*, "Engineering the thermal conductivity along an individual silicon nanowire by selective helium ion irradiation," *Nature communications*, vol. 8*,* p. 15919doi: 10.1038/ncomms15919.

[13] Y. Zhao *et al.*, "Ultralow Thermal Conductivity of Single-Crystalline Porous Silicon Nanowires," *Advanced Functional Materials,* vol. 27, no. 40, p. 1702824, 2017, doi: https://doi.org/10.1002/adfm.201702824.

[14] L. D. Zhao *et al.*, "Ultralow thermal conductivity and high thermoelectric figure of merit in SnSe crystals," (in eng), *Nature,* vol. 508, no. 7496, pp. 373-7, Apr 17 2014, doi: 10.1038/nature13184.

[15] A. Mavrokefalos, N. T. Nguyen, M. T. Pettes, D. C. Johnson, and L. Shi, "In-plane thermal conductivity of disordered layered WSe2 and (W)x(WSe2)y superlattice films," *Applied Physics Letters,* vol. 91, no. 17, 2007, doi: 10.1063/1.2800888.

[16] P. Jiang, X. Qian, X. Gu, and R. Yang, "Probing Anisotropic Thermal Conductivity of Transition Metal Dichalcogenides MX2 (M = Mo, W and X = S, Se) using Time-Domain Thermoreflectance," *Advanced Materials,* vol. 29, no. 36, p. 1701068, 2017, doi: https://doi.org/10.1002/adma.201701068.

[17] M.-J. Lee *et al.*, "Thermoelectric materials by using two-dimensional materials with negative correlation between electrical and thermal conductivity," *Nature Communications,* vol. 7, no. 1, p. 12011, 2016/06/21 2016, doi: 10.1038/ncomms12011.

[18] M. Wolf, R. Hinterding, and A. Feldhoff, "High Power Factor vs. High zT—A Review of Thermoelectric Materials for High-Temperature Application," *Entropy,* vol. 21, no. 11, p. 1058, 2019. [Online]. Available: https://www.mdpi.com/1099-4300/21/11/1058.

[19] Q. Wei *et al.*, "Physics of intrinsic point defects in bismuth oxychalcogenides: A first-principles investigation," *Journal of Applied Physics,* vol. 124, no. 5, p. 055701, 2018, doi: 10.1063/1.5040690.

[20] C. Chen *et al.*, "Electronic structures and unusually robust bandgap in an ultrahigh-mobility layered oxide semiconductor, Bi₂O₂Se," *Science Advances,* vol. 4, no. 9, p. eaat8355, 2018, doi: doi:10.1126/sciadv.aat8355.

[21] Y. Sun, J. Zhang, S. Ye, J. Song, and J. Qu, "Progress Report on Property, Preparation, and Application of Bi2O2Se," *Advanced Functional Materials,* vol. 30, no. 49, p. 2004480, 2020, doi: https://doi.org/10.1002/adfm.202004480.

[22] J. Wu *et al.*, "High electron mobility and quantum oscillations in non-encapsulated ultrathin semiconducting Bi(2)O(2)Se," (in eng), *Nat Nanotechnol,* vol. 12, no. 6, pp. 530-534, Jul 2017, doi: 10.1038/nnano.2017.43.

[23] R. Guo *et al.*, "Electrostatic interaction determines thermal conductivity anisotropy of Bi2O2Se," *Cell Reports Physical Science,* vol. 2, no. 11, p. 100624, 2021/11/17/ 2021, doi: https://doi.org/10.1016/j.xcrp.2021.100624.

[24] F. Yang *et al.*, "Gate-Tunable Polar Optical Phonon to Piezoelectric Scattering in Few-Layer Bi2O2Se for High-Performance Thermoelectrics," *Advanced Materials,* vol. 33, no. 4, p. 2004786, 2021, doi: https://doi.org/10.1002/adma.202004786.

[25] Q. Fu *et al.*, "Ultrasensitive 2D Bi2O2Se Phototransistors on Silicon Substrates," *Advanced Materials,* https://doi.org/10.1002/adma.201804945 vol. 31, no. 1, p. 1804945, 2019/01/01 2019, doi: https://doi.org/10.1002/adma.201804945.

[26] J. Wu *et al.*, "Controlled Synthesis of High-Mobility Atomically Thin Bismuth Oxyselenide Crystals," *Nano Letters,* vol. 17, no. 5, pp. 3021-3026, 2017/05/10 2017, doi: 10.1021/acs.nanolett.7b00335.

[27] A. L. J. Pereira *et al.*, "Experimental and Theoretical Study of Bi2O2Se Under Compression," *The Journal of Physical Chemistry C,* vol. 122, no. 16, pp. 8853-8867, 2018/04/26 2018, doi: 10.1021/acs.jpcc.8b02194.

[28] J. Wu, Y. Chen, J. Wu, and K. Hippalgaonkar, "Perspectives on Thermoelectricity in Layered and 2D Materials," *Advanced Electronic Materials,* vol. 4, no. 12, p. 1800248, 2018, doi: https://doi.org/10.1002/aelm.201800248.

[29] H. K. Ng *et al.*, "Improving carrier mobility in two-dimensional semiconductors with rippled materials," *Nature Electronics,* vol. 5, no. 8, pp. 489-496, 2022/08/01 2022, doi: 10.1038/s41928-022-00777-z.

[30] V. Chen, H. R. Lee, Ç. Köroğlu, C. J. McClellan, A. Daus, and E. Pop, "Ambipolar Thickness-Dependent Thermoelectric Measurements of WSe2," *Nano Letters,* vol. 23, no. 10, pp. 4095-4100, 2023/05/24 2023, doi: 10.1021/acs.nanolett.2c03468.

[31] Z. Yu *et al.*, "Analyzing the Carrier Mobility in Transition-Metal Dichalcogenide MoS2 Field-Effect Transistors," *Advanced Functional Materials,* vol. 27, no. 19, p. 1604093, 2017, doi: https://doi.org/10.1002/adfm.201604093.

[32] N. Ma and D. Jena, "Charge Scattering and Mobility in Atomically Thin Semiconductors," *Physical Review X,* vol. 4, no. 1, p. 011043, 03/18/ 2014, doi: 10.1103/PhysRevX.4.011043.

[33] J. Zhou *et al.*, "Large thermoelectric power factor from crystal symmetry-protected non-bonding orbital in half-Heuslers," *Nature Communications,* vol. 9, no. 1, p. 1721, 2018/04/30 2018, doi: 10.1038/s41467-018-03866-w.

[34] H. E. Ruda, "A theoretical analysis of electron transport in ZnSe," *Journal of Applied Physics,* vol. 59, no. 4, pp. 1220-1231, 1986, doi: 10.1063/1.336509.

[35] N. Maeda, T. Saitoh, K. Tsubaki, T. Nishida, and N. Kobayashi, "Enhanced Electron Mobility in AlGaN/InGaN/AlGaN Double-Heterostructures by Piezoelectric Effect," *Japanese Journal of Applied Physics,* vol. 38, no. 7B, p. L799, 1999/07/01 1999, doi: 10.1143/JJAP.38.L799.

[36] A. Shakouri, "Recent Developments in Semiconductor Thermoelectric Physics and Materials," *Annual Review of Materials Research,* vol. 41, no. 1, pp. 399-431, 2011, doi: 10.1146/annurev-matsci-062910-100445.

[37] Q. Zhu, E. M. Hopper, B. J. Ingram, and T. O. Mason, "Combined Jonker and Ioffe Analysis of Oxide Conductors and Semiconductors," *Journal of the American Ceramic Society,* vol. 94, no. 1, pp. 187-193, 2011, doi: https://doi.org/10.1111/j.1551-2916.2010.04047.x.

[38] G. J. Snyder and E. S. Toberer, "Complex thermoelectric materials," *Nature Materials,* vol. 7, no. 2, pp. 105-114, 2008/02/01 2008, doi: 10.1038/nmat2090.

[39] X. Zhang and Y. Pei, "Manipulation of charge transport in thermoelectrics," *npj Quantum Materials,* vol. 2, no. 1, p. 68, 2017/12/05 2017, doi: 10.1038/s41535-017-0071-2.

[40] B. Zhan, Y. Liu, X. Tan, J.-l. Lan, Y.-h. Lin, and C.-W. Nan, "Enhanced Thermoelectric Properties of Bi2O2Se Ceramics by Bi Deficiencies," *Journal of the American Ceramic Society,* vol. 98, no. 8, pp. 2465-2469, 2015, doi: https://doi.org/10.1111/jace.13619.

[41] X. Tan *et al.*, "Synergistical Enhancement of Thermoelectric Properties in n-Type Bi2O2Se by Carrier Engineering and Hierarchical Microstructure," *Advanced Energy Materials,* vol. 9, no. 31, p. 1900354, 2019, doi: https://doi.org/10.1002/aenm.201900354.

[42] P. Ruleova, C. Drasar, P. Lostak, C. P. Li, S. Ballikaya, and C. Uher, "Thermoelectric properties of Bi2O2Se," *Materials Chemistry and Physics,* vol. 119, no. 1, pp. 299-302, 2010/01/15/ 2010, doi: https://doi.org/10.1016/j.matchemphys.2009.08.067.

[43] M. Kim, D. Park, and J. Kim, "Enhancement of Bi2O2Se thermoelectric power factor via Nb doping," *Journal of Alloys and Compounds,* vol. 851, p. 156905, 2021/01/15/ 2021, doi: https://doi.org/10.1016/j.jallcom.2020.156905.

[44] C. Song, H. Zhou, Y. Gu, L. Pan, C. Chen, and Y. Wang, "Enhanced thermoelectric properties of Bi2O2Se by Bi2Te2.7Se0.3 addition," *Journal of Alloys and Compounds,* vol. 930, p. 167439, 2023/01/05/ 2023, doi: https://doi.org/10.1016/j.jallcom.2022.167439.

[45] Z. Zhou *et al.*, "Advances in n-type Bi2O2Se thermoelectric materials: Progress and perspective," *Materials Today Physics,* vol. 39, p. 101292, 2023/12/01/ 2023, doi: https://doi.org/10.1016/j.mtphys.2023.101292.

[46] L. Pan *et al.*, "Synergistic effect approaching record-high figure of merit in the shear exfoliated n-type Bi2O2-2xTe2xSe," *Nano Energy,* vol. 69, p. 104394, 2020/03/01/ 2020, doi: https://doi.org/10.1016/j.nanoen.2019.104394.

[47] L. Pan *et al.*, "Graphite Nanosheets as Multifunctional Nanoinclusions to Boost the Thermoelectric Performance of the Shear-Exfoliated Bi2O2Se," *Advanced Functional Materials,* vol. 32, no. 30, p. 2202927, 2022, doi: https://doi.org/10.1002/adfm.202202927.